Quantum Variables in Finance and Neuroscience
Lester Ingber • *https://l.ingber.com/lect2018*

qPATHINT LECTURE PLATES

1. Contents & Table of Contents

These lecture plates contain enough detail to be reasonably read as a self-contained paper. Color-coded headers have been added to help identify sub-sections. On request, a black-and-white version is available.

Additional papers and references are at https://www.ingber.com .

$Id: path18_qpathint_lecture,v 1.174 2018/07/13 13:42:07 ingber Exp ingber $

2. Abstract

Background

About 7500 lines of PATHINT C-code, used previously for several systems, has been generalized from 1 dimension to N dimensions, and from classical to quantum systems into qPATHINT processing complex (real + i imaginary) variables. qPATHINT was applied to systems in neocortical interactions and financial options. Classical PATHINT has developed a statistical mechanics of neocortical interactions (SMNI), fit by Adaptive Simulated Annealing (ASA) to Electroencephalographic (EEG) data under attentional experimental paradigms. Classical PATHINT also has demonstrated development of Eurodollar options in industrial applications.

Objective

A study is required to see if the qPATHINT algorithm can scale sufficiently to further develop real-world calculations in these two systems, requiring interactions between classical and quantum scales. A new algorithm also is needed to develop interactions between classical and quantum scales.

Method

Both systems are developed using mathematical-physics methods of path integrals in quantum spaces. Supercomputer pilot studies using XSEDE.org resources tested various dimensions for their scaling limits. For the neuroscience study, neuron-astrocyte-neuron Ca-ion waves are propagated for 100's of msec. A derived expectation of momentum of Ca-ion wave-functions in an external field permits initial direct tests of this approach. For the financial options study, all traded Greeks are calculated for Eurodollar options in quantum-money spaces.

Results

The mathematical-physics and computer parts of the study are successful for both systems. A 3-dimensional path-integral propagation of qPATHINT for is within normal computational bounds on supercomputers. The neuroscience quantum path-integral also has a closed solution at arbitrary time that tests the multiple-scale model including the quantum scale.

Conclusion

Each of the two systems considered contribute insight into applications of qPATHINT to the other system, leading to new algorithms presenting time-dependent propagation of interacting quantum and classical scales. This can be achieved by propagating qPATHINT and PATHINT in synchronous time for the interacting systems.

3. Quantum Computing => Quantum Variables

D-WAVE (Canada)
DeepMind (Canada)
Facebook
Google
IBM
Intel
Microsoft
National Laboratory for Quantum Information Sciences (China)
Nippon Telegraph and Telephone
NOKIA Bell Labs
NSA
Post-Quantum
Rigetti
Russian Quantum Center
Toshiba
Quantum Circuits
Quantum Technologies (European Union)

Error correction a vital consideration for quantum computers
Quantum Computer Calculations => Development of Quantum Variables

4. PATHINT

4.1. Path Integral in Stratonovich (Midpoint) Representation

The path integral in the Feynman (midpoint) representation is most suitable for examining discretization issues in time-dependent nonlinear systems (Langouche *et al*, 1979; Schulman, 1981; Langouche *et al*, 1982). (N.b. $g^{\dagger}$ in DM implies a prepoint evaluation.) Unless explicitly otherwise, the Einstein summation convention is used, wherein repeated indices signify summation; bars $|\cdots|$ imply no summation.

$$P[M_t|M_{t_0}]dM(t) = \int\cdots\int DM \exp\left(-\min\int_{t_0}^{t} dt' L\right)\delta(M(t_0)=M_0)\;\delta(M(t)=M_t)$$

$$DM = \lim_{u\to\infty}\prod_{\rho=1}^{u+1} g^{\dagger 1/2}\prod_{G}(2\pi\theta)^{-1/2}dM_{\rho}^{G}$$

$$L(\dot{M}^{G}, M^{G}, t) = \frac{1}{2}(\dot{M}^{G}-h^{G})g_{GG'}(\dot{M}^{G'}-h^{G'}) + \frac{1}{2}h^{G}{}_{;G} + R/6 - V$$

$$\dot{M}^{G}(t)\to M_{\rho+1}^{G} - M_{\rho}^{G}\;,\; M^{G}(t)\to\frac{1}{2}(M_{\rho+1}^{G}+M_{\rho}^{G})\;,\; [\cdots]_{,G} = \frac{\partial[\cdots]}{\partial M^{G}}$$

$$h^{G} = g^{G} - \frac{1}{2}g^{-1/2}(g^{1/2}g^{GG'})_{,G'}\;,\; h^{G}{}_{;G} = h^{G}_{,G} + \Gamma^{F}_{GF}h^{G} = g^{-1/2}(g^{1/2}h^{G})_{,G}$$

$$g_{GG'} = (g^{GG'})^{-1}\;,\; g = \det(g_{GG'})$$

$$\Gamma^{F}_{JK} \equiv g^{LF}[JK,L] = g^{LF}(g_{JL,K}+g_{KL,J}-g_{JK,L})$$

$$R = g^{JL}R_{JL} = g^{JL}g^{JK}R_{FJKL}$$

$$R_{FJKL} = \frac{1}{2}(g_{FK,JL}-g_{JK,FL}-g_{FL,JK}+g_{JL,FK}) + g_{MN}(\Gamma^{M}_{FK}\Gamma^{N}_{JL}-\Gamma^{M}_{FL}\Gamma^{N}_{JK}) \qquad (1)$$

4.2. Path Integral in Itô (Prepoint) Representation

For conditional probability distributions or for wave functions, in the Itô (prepoint) representation:

$$P[M_t|M_{t_0}]dM(t) = \int \cdots \int DM \exp(-\min \int_{t_0}^{t} dt' L)\delta(M(t_0) = M_0)\delta(M(t) = M_t)$$

$$DM = \lim_{u\to\infty} \prod_{\rho=1}^{u+1} g^{1/2} \prod_{G} (2\pi\Delta t)^{-1/2} dM_\rho^G$$

$$L(\dot{M}^G, M^G, t) = \frac{1}{2}(\dot{M}^G - g^G)g_{GG'}(\dot{M}^{G'} - g^{G'}) + R/6$$

$$\dot{M}^G(t) \to M_{\rho+1}^G - M_\rho^G \ , \ M^G(t) \to M_\rho^G$$

$$g_{GG'} = (g^{GG'})^{-1} \ , \ g = \det(g_{GG'}) \tag{2}$$

Here the diagonal diffusion terms are $g^{|GG|}$ and the drift terms are g^G. If the diffusions terms are not constant, then there are additional terms in the drift, and in a Riemannian-curvature potential $R/6$ for dimension > 1 in the midpoint Stratonovich/Feynman discretization.

4.3. Path-Integral Riemannian Geometry

The midpoint derivation explicitly derives a Riemannian geometry induced by these statistics, with a metric defined by the inverse of the covariance matrix

$$g_{GG'} = (g^{GG'})^{-1} \tag{3}$$

and where R is the Riemannian curvature

$$R = g^{JL} R_{JL} = g^{JL} g^{JK} R_{FJKL} \tag{4}$$

An Itô prepoint discretization for the same probability distribution P gives a much simpler algebraic form,

$$M(\bar{t}_s) = M(t_s)$$

$$\underline{L} = \frac{1}{2} (dM^G/dt - g^G) g_{GG'} (dM^{G'}/dt - g^{G'}) - V \tag{5}$$

but the Lagrangian $\underline{L}$ so specified does not satisfy a variational principle as useful for moderate to large noise; its associated variational principle only provides information useful in the weak-noise limit. Numerically, this often means that finer meshes are required for calculations for the prepoint representation.

4.4. Three Approaches Are Mathematically Equivalent

Three basic different approaches are mathematically equivalent:

(a) Fokker-Planck/Chapman-Kolmogorov partial-differential equations

(b) Langevin coupled stochastic-differential equations

(c) Lagrangian or Hamiltonian path-integrals

The path-integral approach is particularly useful to precisely define intuitive physical variables from the Lagrangian L in terms of its underlying variables M^G:

$$\text{Momentum:}\quad \Pi^G = \frac{\partial L}{\partial(\partial M^G/\partial t)}$$

$$\text{Mass:}\quad g_{GG'} = \frac{\partial L}{\partial(\partial M^G/\partial t)\partial(\partial M^{G'}/\partial t)}$$

$$\text{Force:}\quad \frac{\partial L}{\partial M^G}$$

$$F = ma\text{:}\quad \delta L = 0 = \frac{\partial L}{\partial M^G} - \frac{\partial}{\partial t}\,\frac{\partial L}{\partial(\partial M^G/\partial t)} \tag{6}$$

Differentiation especially of noisy systems often introduces more noise. Integration is inherently a smoothing process, and so the path-integral often gives superior numerical performance.

4.5. Stochastic Differential Equation (SDE)

The Stratonovich (midpoint discretized) Langevin equations can be analyzed in terms of the Wiener process dW^i, which can be rewritten in terms of Gaussian noise $\eta^i = dW^i/dt$ if care is taken in the limit.

$$dM^G = f^G(t, M(t))dt + \hat{g}_i^G(t, M(t))dW^i$$

$$\dot{M}^G(t) = f^G(t, M(t)) + \hat{g}_i^G(t, M(t))\eta^i(t)$$

$$dW^i \to \eta^i dt$$

$$M = \{ M^G; G = 1, \cdots, \Lambda \}$$

$$\eta = \{ \eta^i; i = 1, \cdots, N \}$$

$$\dot{M}^G = dM^G/dt$$

$$< \eta^j(t) >_\eta = 0 \ , < \eta^j(t), \eta^{j'}(t') >_\eta = \delta^{jj'}\delta(t - t') \tag{7}$$

η^i represents Gaussian white noise.

4.6. Partial Differential Equation (PDE)

The Fokker-Planck, or Chapman-Kolmogorov, partial differential equation is:

$$P_{,t} = \frac{1}{2}\,(g^{GG'}P)_{,GG'} - (g^{G}P)_{,G} + VP$$

$$P =< P_{\eta} >_{\eta}$$

$$g^{G} = f^{G} + \frac{1}{2}\,\hat{g}_{i}^{G'}\,\hat{g}_{i,G'}^{G}$$

$$g^{GG'} = \hat{g}_{i}^{G}\,\hat{g}_{i}^{G'}$$

$$(\cdots)_{,G} = \partial(\cdots)/\partial M^{G} \tag{8}$$

g^{G} replaces f^{G} in the SDE if the Itô (prepoint discretized) calculus is used to define that equation. If some boundary conditions are added as Lagrange multipliers, these enter as a ‘‘potential’’ V, creating a Schrödinger-type equation:

4.7. Applications

Path integrals and PATHINT have been applied across several disciplines, including combat simulations (Ingber, Fujio & Wehner, 1991), neuroscience (Ingber, 1994; Ingber & Nunez, 1995; Ingber & Nunez, 2010; Ingber, 2017c; Ingber, 2018), finance (Ingber & Wilson, 2000; Ingber, 2000; Ingber, Chen *et al*, 2001; Ingber, 2016a; Ingber, 2017a; Ingber, 2017b; Ingber, 2017c; Ingber, 2018), and other nonlinear systems (Ingber, 1995a; Ingber, Srinivasan & Nunez, 1996; Ingber, 1998a).

5. Adaptive Simulated Annealing (ASA)

5.1. Importance Sampling

Nonlinear systems present complex spaces, often requiring methods of importance-sampling to scan or to fit parameters. Methods of simulated annealing (SA) are often used. Proper annealing (not "quenching") possesses a proof of finding the deepest minimum in searches.

The ASA code can be downloaded and used without any cost or registration at https://www.ingber.com/#ASA (Ingber, 1993a; Ingber, 2012a).

This algorithm fits empirical data to a theoretical cost function over a D-dimensional parameter space, adapting for varying sensitivities of parameters during the fit.

Heuristic arguments have been developed to demonstrate that this ASA algorithm is faster than the fast Cauchy annealing, $T_i = T_0/k$, and much faster than Boltzmann annealing, $T_i = T_0/\ln k$ (Ingber, 1989).

5.2. Outline of ASA Algorithm

For parameters

$$\alpha_k^i \in [A_i, B_i]$$

sampling with the random variable x^i

$$x^i \in [-1, 1]$$

$$\alpha_{k+1}^i = \alpha_k^i + x^i (B_i - A_i)$$

the default generating function is

$$g_T(x) = \prod_{i=1}^{D} \frac{1}{2 \ln(1 + 1/T_i)(|x^i| + T_i)} \equiv \prod_{i=1}^{D} g_T^i(x^i)$$

in terms of parameter "temperatures"

$$T_i = T_{i0} \exp(-c_i k^{1/D}) \tag{9}$$

It has proven fruitful to use the same type of annealing schedule for the acceptance function h as used for the generating function g, but with the number of acceptance points, instead of the number of generated points, used to determine the k for the acceptance temperature.

All default functions in ASA can be overridden with user-defined functions.

5.3. Hills and Valleys

It helps to visualize the problems presented by such complex systems as a geographical terrain. For example, consider a mountain range, with two "parameters," e.g., along the North–South and East–West directions. We wish to find the lowest valley in this terrain. SA approaches this problem similar to using a bouncing ball that can bounce over mountains from valley to valley.

We start at a high "temperature," where the temperature is an SA parameter that mimics the effect of a fast moving particle in a hot object like a hot molten metal, thereby permitting the ball to make very high bounces and being able to bounce over any mountain to access any valley, given enough bounces. As the temperature is made relatively colder, the ball cannot bounce so high, and it also can settle to become trapped in relatively smaller ranges of valleys. This process is often implemented in qubit-hardware in quantum computers.

We imagine that our mountain range is aptly described by a "cost function." We define probability distributions of the two directional parameters, called generating distributions since they generate possible valleys or states we are to explore.

We define another distribution, called the acceptance distribution, which depends on the difference of cost functions of the present generated valley we are to explore and the last saved lowest valley. The acceptance distribution decides probabilistically whether to stay in a new lower valley or to bounce out of it. All the generating and acceptance distributions depend on temperatures.

5.4. Applications

ASA and its predecessor Very Fas Simulated Reannealing (VFSR) havae been used to fit data by many researchers, including the author in a range of disciplines:

chaotic systems (Ingber, Srinivasan & Nunez, 1996)

combat simulations (Ingber, 1993c; Ingber, 1998a)

financial systems: bonds, equities, futures, options (Ingber, 1990; Ingber, 1996b; Ingber, 2000; Ingber, Chen *et al*, 2001; Ingber & Mondescu, 2003; Ingber, 2005)

neuroscience (Ingber, 1991; Ingber, 1992; Ingber & Nunez, 1995; Ingber, Srinivasan & Nunez, 1996; Ingber, 1996c; Ingber, 1997b; Ingber, 1998b; Ingber, 2006; Ingber, 2009b; Ingber, 2009a; Ingber & Nunez, 2010; Ingber, 2012b; Ingber, 2012c; Nunez, Srinivasan & Ingber, 2013; Ingber, 2013; Ingber, Pappalepore & Stesiak, 2014; Ingber, 2015)

optimization *per se* (Ingber, 1989; Ingber & Rosen, 1992; Ingber, 1993b; Ingber, 1996a; Atiya *et al*, 2003; Ingber, 2012a)

6. Statistical Mechanics of Neocortical Interactions (SMNI)

The project Statistical Mechanics of Neocortical Interactions (SMNI) has been developed in over 30+ papers since 1981, scaling aggregate synaptic interactions to describe neuronal firings, then scaling minicolumnar-macrocolumnar columns of neurons to mesocolumnar dynamics, and then scaling columns of neuronal firings to regional (sensory) macroscopic sites identified in electroencephalographic (EEG) studies (Ingber, 1981; Ingber, 1982; Ingber, 1983; Ingber, 1984; Ingber, 1985b; Ingber, 1994).

The measure of the success of SMNI has been to discover agreement/fits with experimental data from various modeled aspects of neocortical interactions, e.g., properties of short-term memory (STM) (Ingber, 2012b), including its capacity (auditory 7 ± 2 and visual 4 ± 2) (Ericsson & Chase, 1982; G. Zhang & Simon, 1985), duration, stability , primacy versus recency rule, as well other phenomenon, e.g., Hick's law (Hick, 1952; Jensen, 1987; Ingber, 1999), nearest-neighbor minicolumnar interactions within macrocolumns calculating rotation of images, etc (Ingber, 1982; Ingber, 1983; Ingber, 1984; Ingber, 1985b; Ingber, 1994). SMNI was also scaled to include mesocolumns across neocortical regions to fit EEG data (Ingber, 1997b; Ingber, 1997a; Ingber, 2012b).

6.1. Human Neuronal Networks

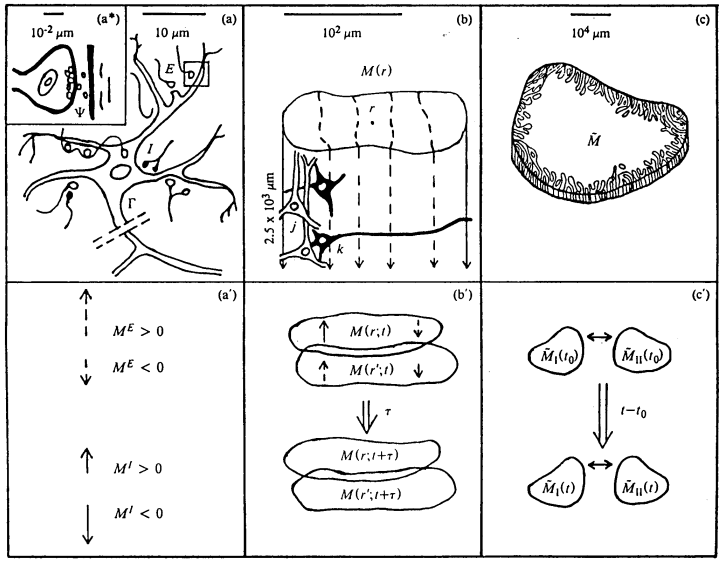

Fig. 1. Three SMNI biophysical scales (Ingber, 1982; Ingber, 1983): (a)-(a*)-(a') microscopic neurons; (b)-(b') mesocolumnar domains; (c)-(c') macroscopic regions.
(a*): synaptic inter-neuronal interactions, averaged over by mesocolumns, are phenomenologically described by the mean and variance of a distribution Ψ (a): intraneuronal transmissions phenomenologically described by the mean and variance of Γ
(a'): collective mesocolumnar-averaged inhibitory (I) and excitatory (E) neuronal firings M
(b): vertical organization of minicolumns together with their horizontal stratification, yielding a physiological entity, the mesocolumn (b'): overlap of interacting mesocolumns at locations r and r' from times t and $t+\tau$, τ on the order of 10 msec
(c): macroscopic regions of neocortex arising from many mesocolumnar domains (c'): regions coupled by long−ranged interactions

6.2. Model of Models

Deep Learning (DL) has invigorated AI approaches to parsing data in complex systems, often to develop control processes of these systems. A couple of decades ago, Neural Net AI approaches fell out of favor when concerns were apparent that such approaches offered little guidance to explain the "why" or "how" such algorithms worked to process data, e.g., contexts which were deemed important to deal with future events and outliers, etc.

The success of DL has overshadowed these concerns. However, that should not diminish their importance, especially if such systems are placed in positions to affect lives and human concerns; humans are ultimately responsible for structures they build.

An approach to dealing with these concerns can be called Model of Models (MOM). An argument in favor of MOM is that humans over thousands of years have developed models of reality across many disciplines, e.g., ranging over Physics, Biology, Mathematics, Economics, etc.

A good use of DL might be to process data for a given system in terms of a collection of models, then again use DL to process the models over the same data to determine a superior model of models (MOM). Eventually, large DL (quantum) machines could possess a database of hundreds or thousands of models across many disciplines, and directly find the best (hybrid) MOM for a given system.

In particular, SMNI offers a reasonable model upon which to further develop MOM, wherein multiple scales of observed intereactions are developed.

6.3. SMNI Development

6.3.1. Synaptic Interactions

The derivation of chemical inter-neuronal and electrical intra-neuronal interactions yields a short-time probability distribution of a given neuron firing due to its just-previous interactions with other neurons (Ingber, 1982; Ingber, 1983). Within τ_j~5–10 msec, the conditional probability that neuron j fires ($\sigma_j = +1$) or does not fire ($\sigma_j = -1$), given its previous interactions with k neurons, is

$$p_{\sigma_j} = \Gamma\,\Psi = \frac{\exp(-\sigma_j F_j)}{\exp(F_j) + \exp(-F_j)}$$

$$F_j = \frac{V_j - \sum_k a^*_{jk} v_{jk}}{(\pi \sum_{k'} a^*_{jk'} (v_{jk'}{}^2 + \phi_{jk'}{}^2))^{1/2}}$$

$$a_{jk} = \frac{1}{2} A_{|jk|}(\sigma_k + 1) + B_{jk} \tag{10}$$

Γ represents the "intra-neuronal" probability distribution, e.g., of a contribution to polarization achieved at an axon given activity at a synapse, taking into account averaging over different neurons, geometries, etc. Ψ represents the "inter-neuronal" probability distribution, e.g., of thousands of quanta of neurotransmitters released at one neuron's postsynaptic site effecting a (hyper-)polarization at another neuron's presynaptic site, taking into account interactions with neuromodulators, etc. This development is true for Γ Poisson, and for Ψ Poisson or Gaussian.

V_j is the depolarization threshold in the somatic-axonal region, v_{jk} is the induced synaptic polarization of E or I type at the axon, and ϕ_{jk} is its variance. The efficacy a_{jk}, related to the inverse conductivity across synaptic gaps, is composed of a contribution A_{jk} from the connectivity between neurons which is activated if the impinging k-neuron fires, and a contribution B_{jk} from spontaneous background noise.

6.3.2. Neuronal Interactions

The microscopic synaptic scale is aggregated up to the mesoscopic scale, using

$$P = \prod_G P^G[M^G(r;t+\tau)|M^{\bar{G}}(r';t)]$$

$$= \sum_{\sigma_j} \delta\left(\sum_{jE}\sigma_j - M^E(r;t+\tau)\right)\delta\left(\sum_{jI}\sigma_j - M^I(r;t+\tau)\right)\prod_j^N p_{\sigma_j} \tag{11}$$

where M represents a mesoscopic scale of columns of N neurons, with subsets E and I, represented by p_{q_i}, constrained by the "delta"-functions δ, representing an aggregate of many neurons in a column. G is used to represent excitatory (E) and inhibitory (I) contributions. $\bar{G}$ designates contributions from both E and I.

In the limit of many neurons per minicolumn, a path integral is derived with mesoscopic Lagrangian L, defining the short-time probability distribution of firings in a minicolumn, composed of ~10^2 neurons, given its just previous interactions with all other neurons in its macrocolumnar surround.

6.3.3. Columnar Interactions

The SMNI Lagrangian L in the prepoint (Itô) representation is

$$L = \sum_{G,G'} (2N)^{-1} (\dot{M}^G - g^G) g_{GG'} (\dot{M}^{G'} - g^{G'}) / (2N\tau) - V'$$

$$g^G = -\tau^{-1} (M^G + N^G \tanh F^G)$$

$$g^{GG'} = (g_{GG'})^{-1} = \delta_G^{G'} \tau^{-1} N^G \mathrm{sech}^2 F^G$$

$$g = \det(g_{GG'}) \tag{12}$$

The threshold factor F^G is derived as

$$F^G = \sum_{G'} \frac{v^G + v^{\ddagger E'}}{\left((\pi/2)[(v_{G'}^G)^2 + (\phi_{G'}^G)^2](\delta^G + \delta^{\ddagger E'}) \right)^{1/2}}$$

$$v^G = V^G - a_{G'}^G v_{G'}^G N^{G'} - \frac{1}{2} A_{G'}^G v_{G'}^G M^{G'} \ , \ v^{\ddagger E'} = -a_{E'}^{\ddagger E} v_{E'}^E N^{\ddagger E'} - \frac{1}{2} A_{E'}^{\ddagger E} v_{E'}^E M^{\ddagger E'}$$

$$\delta^G = a_{G'}^G N^{G'} + \frac{1}{2} A_{G'}^G M^{G'} \ , \ \delta^{\ddagger E'} = a_{E'}^{\ddagger E} N^{\ddagger E'} + \frac{1}{2} A_{E'}^{\ddagger E} M^{\ddagger E'}$$

$$a_{G'}^G = \frac{1}{2} A_{G'}^G + B_{G'}^G \ , \ a_{E'}^{\ddagger E} = \frac{1}{2} A_{E'}^{\ddagger E} + B_{E'}^{\ddagger E} \tag{13}$$

where $A_{G'}^G$ is the columnar-averaged direct synaptic efficacy, $B_{G'}^G$ is the columnar-averaged background-noise contribution to synaptic efficacy. $A_{G'}^G$ and $B_{G'}^G$ have been scaled by $N^*/N \approx 10^3$ keeping F^G invariant. The "‡" parameters arise from regional interactions across many macrocolumns.

6.3.4. SMNI Parameters From Experiments

All values of parameters and their bounds are taken from experimental data, not arbitrarily fit to specific phenomena.

$N^G = \{N^E = 160,\ N^I = 60\}$ was chosen for visual neocortex, $\{N^E = 80,\ N^I = 30\}$ was chosen for all other neocortical regions, $M^{G'}$ and $N^{G'}$ in F^G are afferent macrocolumnar firings scaled to efferent minicolumnar firings by $N/N^* \approx 10^{-3}$, and N^* is the number of neurons in a macrocolumn, about 10^5. V' includes nearest-neighbor mesocolumnar interactions. τ is usually considered to be on the order of 5−10 ms.

Other values also are consistent with experimental data, e.g., $V^G = 10$ mV, $v^G_{G'} = 0.1$ mV, $\phi^G_{G'} = 0.03^{1/2}$ mV.

Nearest-neighbor interactions among columns give dispersion relations that were used to calculate speeds of visual rotation.

The variational principal applied to the SMNI Lagrangian also has been used to derive the wave equation cited by EEG theorists, permitting fits of SMNI to EEG data (Ingber, 1995b).

Note the audit trail of synaptic parameters from synaptic statistics within a neuron to the statistically averaged regional SMNI Lagrangian.

6.4. Previous Applications

6.4.1. Verification of basic SMNI Hypothesis

Only circa 2012 has the core SMNI hypothesis since circa 1980 (Ingber, 1981; Ingber, 1982; Ingber, 1983), that highly synchronous patterns of neuronal firings in fact process high-level information, been verified experimentally (Asher, 2012; Salazar *et al*, 2012).

6.4.2. SMNI Calculations of Short-Term Memory (STM)

SMNI calculations agree with observations (Ingber, 1982; Ingber, 1983; Ingber, 1984; Ingber, 1985b; Ingber, 1994; Ingber, 1995c; Ingber, 1997b; Ingber, 1999; Ingber, 2011; Ingber, 2012b; Ingber, 2012c; Nunez, Srinivasan & Ingber, 2013; Ingber, Pappalepore & Stesiak, 2014; Ingber, 2015; Ingber, 2016b; Ingber, 2017a; Ingber, 2017c): This list includes:

capacity (auditory 7 ± 2 and visual 4 ± 2) (Ingber, 1984)

duration (Ingber, 1985b)

stability (Ingber, 1985b)

primacy versus recency rule (Ingber, 1985b; Ingber, 1985c)

Hick's law (reaction time and g factor) (Ingber, 1999)

nearest-neighbor minicolumnar interactions => rotation of images (Ingber, 1982; Ingber, 1983)

derivation of basis for EEG (Ingber, 1985a; Ingber, 1995b)

6.4.2.1. Three Basic SMNI Models

Three basic models were developed with slight adjustments of the parameters, changing the firing component of the columnar-averaged efficacies $A^G_{G'}$ within experimental ranges, which modify F^G threshold factors to yield in the conditional probability:

(a) case EC, dominant excitation subsequent firings

(b) case IC, inhibitory subsequent firings

(c) case BC, balanced between EC and IC

Consistent with experimental evidence of shifts in background synaptic activity under conditions of selective attention, a Centering Mechanism (CM) on case BC yields case BC′ wherein the numerator of F^G only has terms proportional to $M^{E'}$, $M^{I'}$ and $M^{\ddagger E'}$, i.e., zeroing other constant terms by resetting the background parameters $B^G_{G'}$, still within experimental ranges. This has the net effect of bringing in a maximum number of minima into the physical firing M^G-space. The minima of the numerator then defines a major parabolic trough,

$$A^E_E M^E - A^E_I M^I = 0 \tag{14}$$

about which other SMNI nonlinearities bring in multiple minima calculated to be consistent with STM phenomena.

In recent projects a Dynamic CM (DCM) model is used as well, wherein the $B^G_{G'}$ are reset every few epochs of τ. Such changes in background synaptic activity are seen during attentional tasks (Briggs *et al*, 2013).

6.4.2.2. PATHINT STM

The evolution of a Balanced Centered model (BC) after 500 foldings of $\Delta t = 0.01$, or 5 unit of relaxation time τ exhibits the existence of ten well developed peaks or possible trappings of firing patterns.

This describes the "7 ± 2" rule.

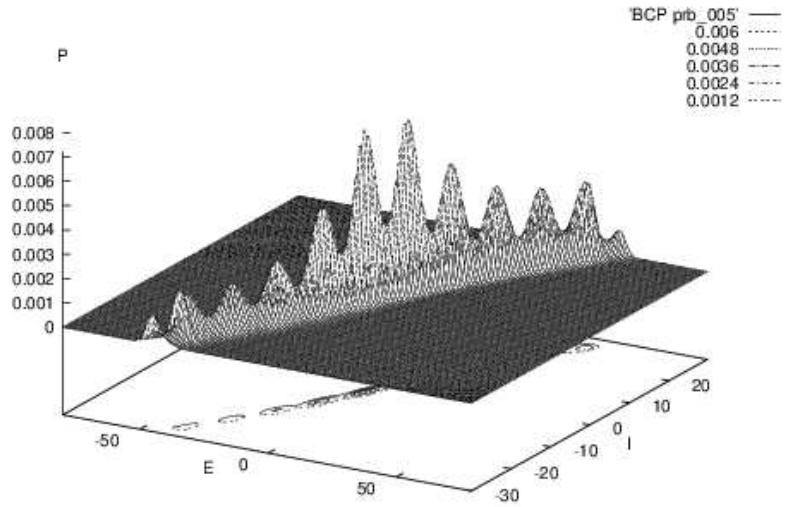

Fig. 2. SMNI STM Model BC at the evolution at 5τ (Ingber & Nunez, 1995).

6.4.2.3. PATHINT STM Visual

The evolution of a Balanced Centered Visual model (BCV) after 1000 foldings of $\Delta t = 0.01$, or 10 unit of relaxation time τ exhibits the existence of four well developed peaks or possible trappings of firing patterns. Other peaks at lower scales are clearly present, numbering on the same order as in the BC' model, as the strength in the original peaks dissipates throughout firing space, but these are much smaller and therefore much less probable to be accessed.

This describes the "4 ± 2" rule for visual STM.

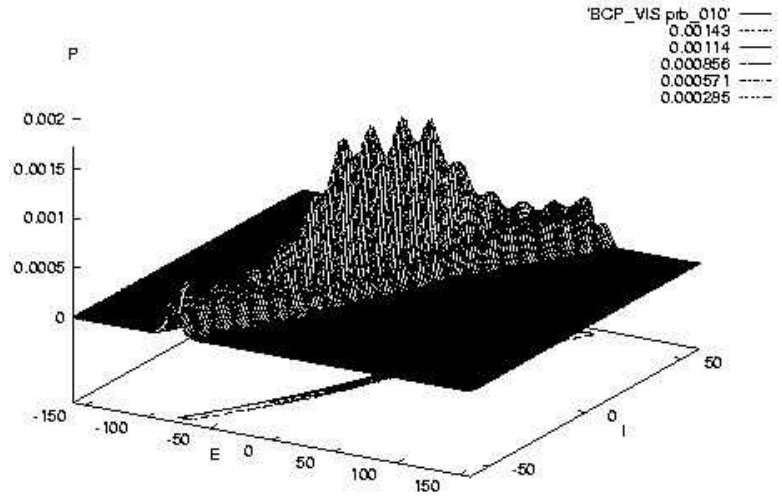

Fig. 3. SMNI STM Model BCV at the evolution at 10τ (Ingber & Nunez, 1995).

6.5. Tripartite Synaptic Interactions

The human brain contains over 10^{11} cells, about half of which are neurons, and the other half are glial cells. Astrocytes comprise a good fraction of glial cells, possibly the majority. Many papers examine the influence of astrocytes on synaptic processes (Bellinger, 2005; Innocenti *et al*, 2000; Scemes & Giaume, 2006; Agulhon *et al*, 2008; Pereira & Furlan, 2009; Reyes & Parpura, 2009; Araque & Navarrete, 2010; Banaclocha *et al*, 2010; Volterra *et al*, 2014).

http://www.astrocyte.info claims:

> They are the most numerous cells in the human brain. [...] Astrocytes outnumber neurons 50:1 and are very active in the central nervous system, unlike previous ideology of astrocytes being "filler" cells.

Glutamate release from astrocytes through a Ca^{2+}-dependent mechanism can activate receptors located at the presynaptic terminals. Regenerative intercellular calcium waves (ICWs) can travel over 100s of astrocytes, encompassing many neuronal synapses. These ICWs are documented in the control of synaptic activity. Glutamate is released in a regenerative manner, with subsequent cells that are involved in the calcium wave releasing additional glutamate (Ross, 2012).

$[Ca^{2+}]$ affect increased release probabilities at synaptic sites, likely due to triggering release of gliotransmitters. (Free Ca^{2+} waves are considered here, not intracellular astrocyte calcium waves in situ which also increase neuronal firings.)

Free regenerative Ca^{2+} waves, arising from astrocyte-neuron interactions, couple to the magnetic vector potential $\mathbf{A}$ produced by highly synchronous collective firings, e.g., during selective attention tasks, as measured by EEG.

6.5.1. Canonical Momentum $\Pi = \mathbf{p} + q\mathbf{A}$

As derived in the Feynman (midpoint) representation of the path integral, the canonical momentum, Π, describes the dynamics of a moving particle with momentum $\mathbf{p}$ in an electromagnetic field. In SI units,

$$\Pi = \mathbf{p} + q\mathbf{A} \tag{15}$$

where $q = -2e$ for Ca^{2+}, e is the magnitude of the charge of an electron $= 1.6 \times 10^{-19}$ C (Coulomb), and $\mathbf{A}$ is the electromagnetic vector potential. (In Gaussian units $\Pi = \mathbf{p} + q\mathbf{A}/c$, where c is the speed of light.) $\mathbf{A}$ represents three components of a 4-vector.

Classical-physics and quantum-physics calculations show that the momenta $\mathbf{p}$ of Ca^{2+} waves is comparable to $q\mathbf{A}$.

Recently work has included classical SMNI calculations of tripartite (neuron-astrocyte-neuron) interactions via Ca^{2+} Waves. Calculations are in progress using interactions between quantum tripartite interactions with classical SMNI models of highly synchronous neuronal firings.

6.5.2. Vector Potential of Wire

A columnar firing state is modeled as a wire/neuron with current **I** measured in A = Amperes = C/s,

$$\mathbf{A}(t) = \frac{\mu}{4\pi} \int \frac{dr}{r} \mathbf{I} \tag{16}$$

along a length z observed from a perpendicular distance r from a line of thickness r_0. If far-field retardation effects are neglected, this yields

$$\mathbf{A} = \frac{\mu}{4\pi} \mathbf{I} \log(\frac{r}{r_0}) \tag{17}$$

where μ is the magnetic permeability in vacuum = $4\pi 10^{-7}$ H/m (Henry/meter). Note the insensitive log dependence on distance; this log factor is taken to be of order 1.

The contribution to **A** includes many minicolumnar lines of current from 100's to 1000's of macrocolumns, within a region not large enough to include many convolutions, but contributing to large synchronous bursts of EEG.

Electric **E** and magnetic **B** fields, derivatives of **A** with respect to r, do not possess this logarithmic insensitivity to distance, and therefore they do not linearly accumulate strength within and across macrocolumns.

Reasonable estimates of contributions from synchronous contributions to P300 measured on the scalp give tens of thousands of macrocolumns on the order of a 100 to 100's of cm^2, while electric fields generated from a minicolumn may fall by half within 5−10 mm, the range of several macrocolumns.

6.5.3. Effects of Vector Potential on Momenta

The momentum $\mathbf{p}$ for a Ca^{2+} ion with mass $m = 6.6 \times 10^{-26}$ kg, speed on the order of 50 μm/s to 100 μm/s, is on the order of 10^{-30} kg-m/s. Molar concentrations of Ca^{2+} waves, comprised of tens of thousands of free ions representing about 1% of a released set, most being buffered, are within a range of about 100 μm to as much as 250 μm, with a duration of more than 500 ms, and concentrations $[Ca^{2+}]$ ranging from 0.1–5 μM (μM = 10^{-3} mol/m^3).

The magnitude of the current is taken from experimental data on dipole moments $\mathbf{Q} = |\mathbf{I}|z$ where $\hat{\mathbf{z}}$ is the direction of the current $\mathbf{I}$ with the dipole spread over z. $\mathbf{Q}$ ranges from 1 pA-m = 10^{-12} A-m for a pyramidal neuron (Murakami & Okada, 2006), to 10^{-9} A-m for larger neocortical mass (Nunez & Srinivasan, 2006). These currents give rise to $q\mathbf{A}$~10^{-28} kg-m/s. The velocity of a Ca^{2+} wave can be ~20–50 μm/s. In neocortex, a typical Ca^{2+} wave of 1000 ions, with total mass $m = 6.655 \times 10^{-23}$ kg times a speed of ~20–50 μm/s, gives $\mathbf{p}$~10^{-27} kg-m/s.

Taking 10^4 synchronous firings in a macrocolumn, leads to a dipole moment $|\mathbf{Q}| = 10^{-8}$ A-m. Taking z to be 10^2 μm = 10^{-4} m, a couple of neocortical layers, gives $|q\mathbf{A}| \approx 2 \times 10^{-19} \times 10^{-7} \times 10^{-8}/10^{-4} = 10^{-28}$ kg-m/s,

6.5.4. Reasonable Estimates

Estimates used here for **Q** come from experimental data, e.g., including shielding and material effects. When coherent activity among many macrocolumns associated with STM is considered, $|\mathbf{A}|$ may be orders of magnitude larger. Since Ca^{2+} waves influence synaptic activity, there is direct coherence between these waves and the activity of **A**.

Classical physics calculates $q\mathbf{A}$ from macroscopic EEG to be on the order of 10^{-28} kg-m/s, while the momentum **p** of a Ca^{2+} ion is on the order of 10^{-30} kg-m/s. This numerical comparison illustrates the importance of the influence of **A** on **p** at classical scales.

The Extreme Science and Engineering Discovery Environment (XSEDE.org) project since February 2013, "Electroencephalographic field influence on calcium momentum waves," fit the SMNI model to EEG data, wherein ionic Ca^{2+} momentum-wave effects among neuron-astrocyte-neuron tripartite synapses modified parameterization of background SMNI parameters. Direct calculations in classical and quantum physics supported the concept that the vector magnetic potential of EEG from highly synchronous firings, e.g., as measured during selective attention, might directly interact with these momentum-waves, thereby creating feedback between these ionic/quantum and macroscopic scales (Ingber, 2012b; Ingber, 2012c; Nunez, Srinivasan & Ingber, 2013; Ingber, Pappalepore & Stesiak, 2014; Ingber, 2015; Ingber, 2016b; Ingber, 2017a).

6.6. Comparing Testing Data with Training Data

Using data from http://physionet.nlm.nih.gov/pn4/erpbci , SMNI was fit to highly synchronous waves (P300) during attentional tasks, for each of 12 subjects, it was possible to find 10 Training runs and 10 Testing runs (Goldberger *et al*, 2000; Citi *et al*, 2010).

Spline-Laplacian transformations on the EEG potential Φ are proportional to the SMNI M^G firing variables at each electrode site. The electric potential Φ is experimentally measured by EEG, not $\mathbf{A}$, but both are due to the same currents $\mathbf{I}$. Therefore, $\mathbf{A}$ is linearly proportional to Φ with a simple scaling factor included as a parameter in fits to data. Additional parameterization of background synaptic parameters, $B^G_{G'}$ and $B^{\ddagger E}_{E'}$, modify previous work.

The $\mathbf{A}$ model outperformed the no-$\mathbf{A}$ model, where the no-$\mathbf{A}$ model simply has used $\mathbf{A}$-non-dependent synaptic parameters. Cost functions with an $|\mathbf{A}|$ model were much worse than either the $\mathbf{A}$ model or the no-$\mathbf{A}$ model. Runs with different signs on the drift and on the absolute value of the drift also gave much higher cost functions than the $\mathbf{A}$ model.

7. Statistical Mechanics of Financial Markets (SMFM)

7.1. Quantum Money and Blockchains

Quantum computing is here, and in the near future it will be applied to financial products, e.g., blockchains. It is not very far-fetched to assume that soon there will be financial derivatives developed on these products. Then, as is the case in classical real spaces with PATHTREE and PATHINT, qPATHTREE and qPATHINT are now poised to calculate financial derivatives in quantum complex spaces. This is beyond simply using quantum computation of financial derivatives, since the space of the dependent variables themselves may live in quantum worlds.

The marketplace will determine traded variables: For example, consider VIX, as a proxy for Volatility of Volatility of specific markets, is not the same as Volatility of Volatility for a single market, but exchanges list VIX.

7.2. Previous Applications — PATHINT

Options V are generally described by a portfolio Π over an underlying asset S, where the real-world probability distribution of S often is critical to numerical details for trading. The asset is often hedged by trading the option V and a quantity Δ of the asset S.

$$d\Pi = \sigma\left(\frac{\partial V}{\partial S} - \Delta\right) dX + \left(\mu S \frac{\partial V}{\partial S} + \frac{1}{2}\sigma^2 S^2 \frac{\partial^2 V}{\partial S^2} + \frac{\partial V}{\partial t} - \mu\Delta S\right) dt$$

$$\Gamma = \frac{\partial^2 \Pi}{\partial S^2}\ ,\ \Theta = \frac{\partial \Pi}{\partial t}\ ,\ \Upsilon = \frac{\partial \Pi}{\partial \sigma}\ ,\ \rho = \frac{\partial \Pi}{\partial r} \tag{18}$$

The portfolio Π to be hedged is often considered to be "risk-neutral," if Δ is chosen such that $\Delta = \frac{\partial V}{\partial S}$.

While quite a few closed-form solutions exist for European options (Black & Scholes, 1973), where there is not early exercise, for American options — among the most popular options — there is no general closed form, and numerical calculations must be performed (Hull, 2000). In the path-integral approach, first the probability "tree" for S is propagated forward in time until the expiration date T, branching out as extended S values develop.

Then, marching back in time, at each time-node various calculations can be performed, e.g., the Greeks above, inserting changes (often "shocks") in dividends, interest rates, changes in cheapest-to-deliver of a basket of bonds in the case of options on bond futures, etc (Ingber & Wilson, 1999; Ingber, 2000).

Explicitly, at each node a calculation is performed, comparing the strike price X to the price S at that node, and a decision is made, e.g., whether to exercise the option at that node — determining the fair value of the option price V. To obtain the Greeks above, most derivatives of these Derivatives are calculated numerically by using values across branches and notes.

7.2.1. Volatility of Volatility of American Options

An example of a two-dimensional options model processed by PATHINT developed the volatility of volatility of options on Eurodollars, using 2-factor model developed by the author:

$$dS = \mu\, S\, dt + \sigma\, F(S, S_0, S_\infty, x, y)\, dz_S$$

$$d\sigma = \nu\, dt + \varepsilon\, dz_\sigma$$

$$F(S, S_0, S_\infty, x, y) = \begin{cases} S, & S < S_0 \\ S^x S_0^{1-x}, & S_0 \le S \le S_\infty \\ S^y S_0^{1-x} S_\infty^{x-y}, & S > S_\infty \end{cases} \tag{19}$$

where S_0 and S_∞ are selected to lie outside the data region used to fit the other parameters, e.g., $S_0 = 1/2$ and $S_\infty = 20$ for fits to Eurodollar futures which historically have a very tight range relative to other markets.

7.2.1.1. SMFM Example of 2-Factor PATHINT

An example of a two-factor distribution evolved out to $T = 0.5$ year for $x = 0.7$ simply shows PATHINT at work.

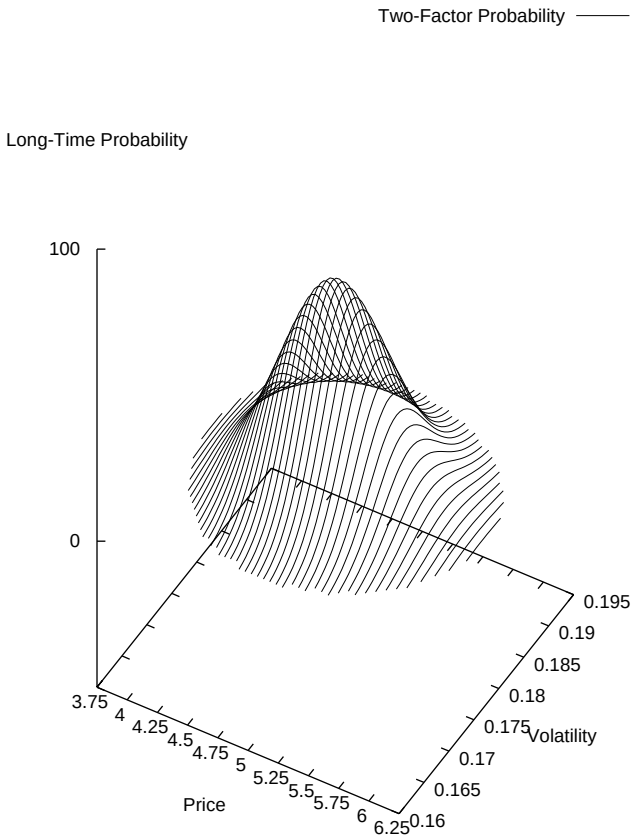

Fig. 4. A two-factor distribution evolved out to $T = 0.5$ year for $x = 0.7$ (Ingber, 2000).

7.3. Application to Risk

As an aside, path integrals also have been applied to copula risk management. The approach to consider a basket of markets (a few, or thousands of markets) in their **dx** variables, each fit separately to real data, e.g., using a parameterized 2-tail exponential distribution. Then each market is transformed to a Gaussian distribution in their **dy** variables, and the collection of Gaussians now permits a multi-factor Gaussian to be developed from which meaningful considerations based on covariance can be based, e.g., for value at risk (VaR).

This gives a multivariate correlated process P in the dy variables, in terms of Lagrangians L and Action A,

$$P(dy) \equiv P(dy^1, \ldots, dy^N) = (2\pi dt)^{-\frac{N}{2}} g^{-\frac{1}{2}} \exp(-Ldt) \tag{20}$$

The Lagrangian L is

$$L = \frac{1}{2dt^2} \sum_{ij} dy^i g_{ij} dy^j \tag{21}$$

The effective action A_{eff}, presenting a "cost function" useful for sampling and optimization, is defined by

$$P(dy) = \exp(-A_{eff})$$

$$A_{eff} = Ldt + \frac{1}{2} \ln g + \frac{N}{2} \ln(2\pi dt) \tag{22}$$

7.3.1. Copula

The multivariate distribution in x-space is specified, including correlations, using

$$P(dx) = P(dy) \left| \frac{\partial\, dy^i}{\partial\, dx^j} \right| \tag{23}$$

where $\left| \frac{\partial dy^i}{\partial dx^j} \right|$ is the Jacobian matrix specifying this transformation. This yields

$$P(dx) = g^{-\frac{1}{2}} \exp\left(-\frac{1}{2} \sum_{ij} (dy^i_{dx})^\dagger (g_{ij} - I_{ij}) (dy^j_{dx}) \right) \prod_i P_i(dx^i) \tag{24}$$

where (dy_{dx}) is the column-vector of $(dy^1_{dx}, \cdots, dy^N_{dx})$ expressed back in terms of their respective $(dx^1, \ldots, dx^N)$, $(dy_{dx})^\dagger$ is the transpose row-vector, and (I) is the identity matrix.

The Gaussian copula $C(dx)$ is defined by

$$C(dx) = g^{-\frac{1}{2}} \exp\left(-\frac{1}{2} \sum_{ij} (dy^i_{dx})^\dagger (g_{ij} - I_{ij}) (dy^j_{dx}) \right) \tag{25}$$

Some additional work is performed to generate guaranteed stable numerical covariance matrices.

These calculations have been embedded as a middle layer in a program Trading in Risk Dimensions (TRD). An inner-shell of Canonical Momenta Indicators (CMI), momenta Π defined previously, is adaptively fit to incoming market data. A parameterized trading-rule outer-shell uses ASA to fit the trading system to historical data. An additional risk-management middle-shell is added to create a three-shell recursive optimization/sampling/fitting algorithm. Portfolio-level distributions of copula-transformed multivariate distributions are generated by Monte Carlo samplings. ASA is used to importance-sample weightings of these markets.

8. qPATHINT: Inclusion of Quantum Scales

8.1. PATHINT/qPATHINT Code

To numerically calculate the path integral, especially for serial changes in time — not approachable with standard Monte Carlo techniques — PATHINT was developed. the PATHINT C code of about 7500 lines of code was rewritten for the GCC C-compiler to use double complex variables instead of double variables. The code is written for arbitrary N dimensions. The outline of the code is described here for classical or quantum systems, using generic coordinates q and x (Ingber, 2016a; Ingber, 2017a; Ingber, 2017b):

This histogram procedure recognizes that the distribution (probabilities for classical systems, wave-functions for quantum systems) can be numerically approximated to a high degree of accuracy by sums of rectangles of height P_i and width Δq^i at points q^i.

8.1.1. Shocks

Many real-world systems propagate in the presence of continual "shocks":

8.1.1.1. SMNI

regenerative Ca^{2+} waves due to collisions
interactions with changing **A**

8.1.1.2. SMFM

future dividends
changes in interest rates
changes in asset distributions used in American options algorithms

8.1.2. PATHINT/qPATHINT Histograms

Consider a one-dimensional system in variable x, in the prepoint Itô discretization, the path-integral representation can be written in terms of the kernel G, for each of its intermediate integrals, as

$$P(x;t+\Delta t) = \int dx' [g^{1/2}(2\pi\Delta t)^{-1/2} \exp(-L\,\Delta t)] P(x';t) = \int dx' G(x,x';\Delta t) P(x';t)$$

$$P(x;t) = \sum_{i=1}^{N} \pi(x-x^i) P_i(t)$$

$$\pi(x-x^i) = 1\,,\ \ (x^i - \frac{1}{2}\,\Delta x^{i-1}) \le x \le (x^i + \frac{1}{2}\,\Delta x^i)\ ;\ 0\,,\ \ \text{otherwise} \tag{26}$$

This yields

$$P_i(t+\Delta t) = T_{ij}(\Delta t) P_j(t)$$

$$T_{ij}(\Delta t) = \frac{2}{\Delta x^{i-1} + \Delta x^i} \int_{x^i - \Delta x^{i-1}/2}^{x^i + \Delta x^i/2} dx \int_{x^j - \Delta x^{j-1}/2}^{x^j + \Delta x^j/2} dx' G(x,x';\Delta t) \tag{27}$$

T_{ij} is a banded matrix representing the Gaussian nature of the short-time probability centered about the (possibly time-dependent) drift.

Several projects have used this algorithm (Wehner & Wolfer, 1983a; Wehner & Wolfer, 1983b; Wehner & Wolfer, 1987; Ingber & Nunez, 1995; Ingber, Srinivasan & Nunez, 1996; Ingber & Wilson, 1999). Special 2-dimensional codes were developed for specific projects in Statistical Mechanics of Combat (SMC), SMNI and SMFM (Ingber, Fujio & Wehner, 1991; Ingber & Nunez, 1995; Ingber, 2000).

8.1.3. Meshes For [q]PATHINT

Explicit dependence of L on time t also can be included without complications. Care must be used in developing the mesh Δq^i, which is strongly dependent on diagonal elements of the diffusion matrix, e.g.,

$$\Delta q^i \approx (\Delta t g^{|ii|})^{1/2} \tag{28}$$

This constrains the dependence of the covariance of each variable to be a (nonlinear) function of that variable to present a rectangular-ish underlying mesh. Since integration is inherently a smoothing process (Ingber, 1990), fitting the data with integrals over the short-time probability distribution, this permits the use of coarser meshes than the corresponding stochastic differential equation(s) (Wehner & Wolfer, 1983a).

For example, the coarser resolution is appropriate, typically required, for a numerical solution of the time-dependent path integral. By considering the contributions to the first and second moments, conditions on the time and variable meshes can be derived. Thus Δt can be measured by the diffusion divided by the square of the drift.

8.2. Lessons Learned From SMFM and SMNI

8.2.1. Broad-Banded Kernels Required

SMNI => requires broad-banded kernel for oscillatory quantum states

SMFM PATHTREE, and its derived qPATHTREE, is a different options code, based on path-integral error analyses, permitting a new very fast binary calculation, also applied to nonlinear time-dependent systems (Ingber, Chen *et al*, 2001).

However, in contrast to the present PATHINT/qPATHINT code that has been generalized to N dimensions, currently an SMFM [q]PATHTREE is only a binary tree with $J = 1$ and cannot be effectively applied to quantum oscillatory systems (Ingber, 2016a; Ingber, 2017a; Ingber, 2017b).

8.2.2. Calculations At Each Node At Each Time Slice

SMFM => Calculate at Each Node of Each Time Slice — Back in Time

SMNI => Calculate at Each Node of Each Time Slice — Forward in Time
SMNI PATHINT interacts at each time slice with Ca^{2+}-wave qPATHINT.

8.2.3. SMFM qPATHINT With Serial Shocks

UCSD: "Comet is a 2.0 Petaflop (PF) Dell integrated compute cluster, with next-generation Intel Haswell processors (with AVX2), interconnected with Mellanox FDR InfiniBand in a hybrid fat-tree topology. Full bisection bandwidth is available at rack level (72 nodes) and there is a 4:1 oversubscription cross-rack. Compute nodes feature 320 GB of SSD storage and 128GB of DRAM per node."

To appreciate requirements of kernel memory as a function of dimension, some N-dim qPATHINT runs for SMFM were considered in a pilot study, using a contrived N-factor model with the same 1-dimensional system cloned in all dimensions:

D=1:imxall: 27 , jmxall: 7 , ijkcnt: 189
D=2:imxall: 729 , jmxall: 49 , ijkcnt: 35721
D=3:imxall: 19683 , jmxall: 343 , ijkcnt: 6751269
D=4:imxall: 531441 , jmxall: 2401 , ijkcnt: 1275989841
D=5:imxall: 14348907 , jmxall: 16807 , ijkcnt: 241162079949
D=6:imxall: 387420489 , jmxall: 117649 , ijkcnt: 45579633110361
D=7:imxall: 10460353203 , jmxall: 823543 , ijkcnt: 8614550657858229

The kernel size is $(IJ)^N$, where I = imxall, J = jmxall (= kernel band width), and kernel size = ijkcnt. This spatial mesh might change at each time slice.

A full set of ASA fits of classical SMNI to EEG data takes thousands of hours of supercomputer CPUs. Cost functions that include quantum processes will take even longer.

8.3. SMNI

Without random shocks, the wave function ψ_e representing the interaction of the EEG magnetic vector potential $\mathbf{A}$ with the momenta $\mathbf{p}$ of Ca^{2+} wave packets was derived in closed form from the Feynman (midpoint) representation of the path integral using path-integral techniques (Schulten, 1999)

$$\psi_e(t) = \int d\mathbf{r}_0\, \psi_0\, \psi_F = \left[\frac{1 - i\hbar t/(m\Delta\mathbf{r}^2)}{1 + i\hbar t/(m\Delta\mathbf{r}^2)}\right]^{1/4} \left[\pi\Delta\mathbf{r}^2\{1 + [\hbar t/(m\Delta\mathbf{r}^2)]^2\}\right]^{-1/4}$$

$$\times \exp\left[-\frac{[\mathbf{r} - (\Pi_0 + q\mathbf{A})t/m]^2}{2\Delta\mathbf{r}^2}\,\frac{1 - i\hbar t/(m\Delta\mathbf{r}^2)}{1 + [\hbar t/(m\Delta\mathbf{r}^2)]^2} + i\,\frac{\Pi_0\cdot\mathbf{r}}{\hbar} - i\,\frac{(\Pi_0 + q\mathbf{A})^2 t}{2\hbar m}\right]$$

$$\psi_F(t) = \int \frac{d\mathbf{p}}{2\pi\hbar} \exp\left[\frac{i}{\hbar}\left(\mathbf{p}(\mathbf{r} - \mathbf{r}_0) - \frac{\Pi^2 t}{(2m)}\right)\right] = \left[\frac{m}{2\pi i\hbar t}\right]^{1/2} \exp\left[\frac{im(\mathbf{r} - \mathbf{r}_0 - q\mathbf{A}t/m)^2}{2\hbar t} - \frac{i(q\mathbf{A})^2 t}{2m\hbar}\right]$$

$$\psi_0 = \psi(\mathbf{r}_0, t = 0) = \left(\frac{1}{\pi\Delta\mathbf{r}^2}\right)^{1/4} \exp\left(-\frac{\mathbf{r}_0^2}{2\Delta\mathbf{r}^2} + i\,\frac{\Pi_0\cdot\mathbf{r}_0}{\hbar}\right) \tag{29}$$

where ψ_0 is the initial Gaussian packet, ψ_F is the free-wave evolution operator, $\hbar$ is the Planck constant, q is the electronic charge of Ca^{2+} ions, m is the mass of a wave-packet of 1000 Ca^{2+} ions, $\Delta\mathbf{r}^2$ is the spatial variance of the wave-packet, the initial canonical momentum is $\Pi_0 = \mathbf{p}_0 + q\mathbf{A}_0$, and the evolving canonical momentum is $\Pi = \mathbf{p} + q\mathbf{A}$. Detailed calculations show that $\mathbf{p}$ of the Ca^{2+} wave packet and $q\mathbf{A}$ of the EEG field make about equal contributions to Π.

Fits follow the time-dependent EEG data: SMNI synaptic parameters are affected by the model of Ca^{2+} waves. $\mathbf{A}$ derived from the EEG data affects the development of Ca^{2+} waves.

8.3.1. PATHINT SMNI + qPATHINT Ca^{2+} wave-packet

At each node of each time slice, calculate quantum-scale Ca^{2+} wave-packet (2-way) interactions with macroscopic large-scale EEG/**A**.

PATHINT: Classical SMNI Lagrangian
qPATHINT: Quantum Ca^{2+} wave-packet Lagrangian

Sync in time during P300 attentional tasks.
Time/phase relations between classical and quantum systems may be important.
ASA-fit synchronized classical-quantum PATHINT-qPATHINT model to EEG data.
A(EEG) is determined experimentally, and includes all synaptic background $B^G_{G'}$ effects.

Tripartite influence on synaptic $B^G_{G'}$ is measured by the ratio of packet's $< \mathbf{p}(t) >_{\psi^*\psi}$ to $< \mathbf{p}_0(t_0) >_{\psi^*\psi}$ at onset of attentional task. $\mathbf{A} = \sum_R \mathbf{A}_R \ln(R/R_0)$ from all R regions. Here $<>_{\psi^*\psi}$ is taken over $\psi^*_{\rm e}\,\psi_{\rm e}$.

$$< \mathbf{p} >_{\psi^*\psi} = m\,\frac{< \mathbf{r} >_{\psi^*\psi}}{t - t_0} = \frac{q\mathbf{A} + \Pi_0}{m^{1/2}|\Delta\mathbf{r}|}\left(\frac{(\hbar t)^2 + (m\Delta\mathbf{r}^2)^2}{\hbar t + m\Delta\mathbf{r}^2}\right)^{1/2} \tag{30}$$

Note that at $t = 0$, $< \mathbf{p} >_{\psi^*\psi} = q\mathbf{A}$. **A** changes slower than **p**, so static approximation of **A** used to derive $\psi_{\rm e}$ and $< \mathbf{p} >_{\psi^*\psi}$ is reasonable to use within P300 EEG epochs, resetting $t = 0$ at the onset of each classical EEG measurement (1.953 ms apart), using the current **A**. This permits tests of interactions across scales in a classical context.

8.3.1.1. Results Using $< \mathbf{p} >_{\psi^*\psi}$

$< \mathbf{p} >_{\psi^*\psi}$ was used in classical-physics SMNI fits to EEG data using ASA. Training with ASA used 100K generated states over 12 subjects with and without **A**, followed by 1000 generated states with the simplex local code contained with ASA. These calculations directly use $< \mathbf{p} >_{\psi^*\psi}$ from Ca^{2+} wave packets, with one additional parameter across all EEG regions to weight the contribution to synaptic background $B^G_{G'}$.

As with previous studies using this data, results sometimes give Testing cost functions less than the Training cost functions. This reflects on great differences in data, likely from great differences in subjects' contexts, e.g., possibly due to subjects' STM strategies only sometimes including effects calculated here. This confirms the need to further test these multiple-scale models with more EEG data, and with the PATHINT-qPATHINT coupled algorithm described above.

Table 1. Column 1 is the subject number; the other columns are cost functions. Columns 2 and 3 are no-**A** model's Training (TR0) and Testing (TE0). Columns 4 and 5 are **A** model's Training (TR**A**) and Testing (TE**A**). Columns 6 and 7 are switched no-**A** model's Training (sTR0) and Testing (sTE0). Columns 8 and 9 are switched **A** model's Training (sTR**A**) and Testing (sTE**A**).

Sub	TR0	TE0	TR**A**	TE**A**	sTR0	sTE0	sTR**A**	sTE**A**
s01	85.75	121.23	84.76	121.47	120.48	86.59	119.23	87.06
s02	70.80	51.21	68.63	56.51	51.10	70.79	49.36	74.53
s03	61.37	79.81	59.83	78.79	79.20	61.50	75.22	79.17
s04	52.25	64.20	50.09	66.99	63.55	52.83	63.27	64.60
s05	67.28	72.04	66.53	72.78	71.38	67.83	69.60	68.13
s06	84.57	69.72	80.22	64.13	69.09	84.67	61.74	114.21
s07	68.66	78.65	68.28	86.13	78.48	68.73	75.57	69.58
s08	46.58	43.81	44.24	49.38	43.28	47.27	42.89	63.09
s09	47.22	24.88	46.90	25.77	24.68	47.49	24.32	49.94
s10	53.18	33.33	53.33	36.97	33.14	53.85	30.32	55.78
s11	43.98	51.10	43.29	52.76	50.95	44.47	50.25	45.85
s12	45.78	45.14	44.38	46.08	44.92	46.00	44.45	46.56

8.3.2. Quantum Zeno Effects

In the context of quantum mechanics, the wave function of the Ca^{2+} wave packet was calculated, and it was demonstrated that overlap with multiple collisions, due to their regenerative processes, during the observed long durations of hundreds of ms of typical Ca^{2+} waves support a Zeno or "bang-bang" effect which may promote long coherence times (Facchi, Lidar & Pascazio, 2004; Facchi & Pascazio, 2008; Wu *et al*, 2012; Giacosa & Pagliara, 2014; P. Zhang *et al*, 2014; Kozlowski *et al*, 2015; Patil *et al*, 2015; Muller *et al*, 2016).

Of course, the Zeno/"bang-bang" effect may exist only in special contexts, since decoherence among particles is known to be very fast, e.g., faster than phase-damping of macroscopic classical particles colliding with quantum particles (Preskill, 2015).

Here, the constant collisions of Ca^{2+} ions as they enter and leave the Ca^{2+} wave packet due to the regenerative process that maintains the wave, may perpetuate at least part of the wave, permitting the Zeno/"bang-bang" effect. In any case, qPATHINT as used here provides an opportunity to explore the coherence stability of the wave due to serial shocks of this process.

8.3.3. Survival of Wave Packet

In momentum space the wave packet, consider $\phi(\mathbf{p},t)$ being "kicked" from $\mathbf{p}$ to $\mathbf{p}+\delta\mathbf{p}$, and simply assume that random repeated kicks of $\delta\mathbf{p}$ result in $<\delta\mathbf{p}>\approx 0$, and each kick keeps the variance $\Delta(\mathbf{p}+\delta\mathbf{p})^2 \approx \Delta(\mathbf{p})^2$. Then, the overlap integral at the moment t of a typical kick between the new and old state is

$$<\phi^*(\mathbf{p}+\delta\mathbf{p},t)|\phi(\mathbf{p},t)>=\exp\left(\frac{i\kappa+\rho}{\sigma}\right)$$

$$\kappa = 8\delta\mathbf{p}\Delta\mathbf{p}^2\hbar m(q\mathbf{A}+\mathbf{p}_0)t - 4(\delta\mathbf{p}\Delta\mathbf{p}^2 t)^2$$

$$\rho = -(\delta\mathbf{p}\hbar m)^2$$

$$\sigma = 8(\Delta\mathbf{p}\hbar m)^2 \tag{31}$$

where $\phi(\mathbf{p}+\delta\mathbf{p},t)$ is the normalized wave function in $\mathbf{p}+\delta\mathbf{p}$ momentum space. A crude estimate is obtained of the survival time $A(t)$ and survival probability $p(t)$ (Facchi & Pascazio, 2008),

$$A(t) =<\phi^*(\mathbf{p}+\delta\mathbf{p},t)|\phi(\mathbf{p},t)>$$

$$p(t) = |A(t)|^2 \tag{32}$$

8.3.3.1. Calculation of Survival

These numbers yield:

$$< \phi^*(\mathbf{p}+\delta\mathbf{p},t)|\phi(\mathbf{p},t) >= \exp(i(1.67\times10^{-1}t - 1.15\times10^{-2}t^2) - 1.25\times10^{-7}) \quad (33)$$

Even many small repeated kicks do not appreciably affect the real part of ϕ, and these projections do not appreciably destroy the original wave packet, giving a survival probability per kick as $p(t) \approx \exp(-2.5\times10^{-7}) \approx 1 - 2.5\times10^{-7}$.

Both time-dependent phase terms in the exponent are sensitive to time scales on the order of 1/10 s, scales prominent in STM and in synchronous neural firings measured by EEG. This suggests that **A** effects on Ca^{2+} wave functions may maximize their influence on STM at frequencies consistent with synchronous EEG during STM by some mechanisms not yet determined.

All these calculations support this model, in contrast to other models of quantum brain processes without such calculational support (McKemmish *et al*, 2009; Hagan *et al*, 2002; Hameroff & Penrose, 2013).

9. Applications

9.1. SMNI

9.1.1. Nano-Robotic Applications

To highlight the importance of research using nano-robots in the context of this project, there is the potential of carrying pharmaceutical products in nanosystems that could affect unbuffered Ca^{2+} waves in neocortex (Ingber, 2015). A Ca^{2+}-wave momentum-sensor could act like a piezoelectric device.

At the onset of a Ca^{2+} wave (on the order of 100's of ms), a change of momentum can be on the order of 10^{-30} kg-m/s for a typical Ca^{2+} ion. For a Ca^{2+} wave packet of 1000 ions with onset time of 1 ms, this gives a force on the order of 10^{-24} N (1 N $\equiv$ 1 Newton = 1 kg-m/s^2). The nanosystem would be attracted to this site, depositing chemicals/drugs that interact with the regenerative Ca^{2+}-wave process.

If the receptor area of the nanosystem were 1 nm^2 (the resolution of scanning confocal electron microscopy (SCEM)), this would require an extreme pressure sensitivity of 10^{-6} Pa (1 Pa = 1 pascal = 1 N/m^2).

The nanosystem could be switched on/off at a regional/columnar level by sensitivity to local electric/magnetic fields. Thus, piezoelectric nanosystems can affect background/noise efficacies at synaptic gaps via control of Ca^{2+} waves, affecting highly synchronous firings which carry many STM processes, which in turn affect the influence of of Ca^{2+} waves via the vector potential $\mathbf{A}$, etc.

9.1.2. Free Will

In addition to the intrinsic interest of researching STM and multiple scales of neocortical interactions via EEG data, there is interest in researching possible quantum influences on highly synchronous neuronal firings relevant to STM to understand possible connections to consciousness and "Free Will" (FW) (Ingber, 2016a; Ingber, 2016b).

If neuroscience ever establishes experimental feedback from quantum-level processes of tripartite neuron-astrocyte-neuron synaptic interactions with large-scale synchronous neuronal firings, that are now recognized as being highly correlated with STM and states of attention, then FW may yet be established using the Conway-Kochen quantum no-clone "Free Will Theorem" (FWT) (Conway & Kochen, 2006; Conway & Kochen, 2009).

Basically, this means that a Ca^{2+} quantum wave-packet may generate a state proven to have not previously existed; quantum states cannot be cloned.

9.2. SMFM

9.2.1. Enhanced Security/Verification

As in SMNI, here too the core of the quantum no-clone "Free Will Theorem" (FWT) theorem can have important applications. Quantum currency cannot be cloned. Such currencies are exceptional candidates for very efficient blockchains, e.g., since each "coin" has a unique identity (Meyer, 2009; Aaronson & Christiano, 2012; Bartkiewicz *et al*, 2016; Jogenfors, 2016).

As in SMNI, here too there are issues about the decoherence time of such "coins".

10. Acknowledgments

The author thanks the Extreme Science and Engineering Discovery Environment (XSEDE.org), for supercomputer grants since February 2013, starting with "Electroencephalographic field influence on calcium momentum waves", one under PHY130022 and two under TG-MCB140110. The current grant under TG-MCB140110, "Quantum path-integral qPATHTREE and qPATHINT algorithms", was started in 2017, and renewed through December 2018. XSEDE grants have spanned several projects described in
https://www.ingber.com/lir_computational_physics_group.html .

11. References

S. Aaronson & P. Christiano (2012) Quantum money from hidden subspaces. arXiv:1203.4740 [quant-ph]. MIT.

C. Agulhon, J. Petravicz, A.B. McMullen, E.J. Sweger, S.K. Minton, S.R. Taves, K.B. Casper, T.A. Fiacco & K.D. McCarthy (2008) What is the role of astrocyte calcium in neurophysiology?. Neuron. 59, 932-946.

A. Araque & M. Navarrete (2010) Glial cells in neuronal network function. Philosphical Transactions of The Royal Society B. , 2375-2381.

J. Asher (2012) Brain's code for visual working memory deciphered in monkeys NIH-funded study. NIH Press Release. NIH. [URL http://www.nimh.nih.gov/news/science-news/2012/in-sync-brain-waves-hold-memory-of-objects-just-seen.shtml]

A.F. Atiya, A.G. Parlos & L. Ingber (2003) A reinforcement learning method based on adaptive simulated annealing, In: Proceedings International Midwest Symposium on Circuits and Systems (MWCAS), December 2003, IEEE CAS. [URL https://www.ingber.com/asa03_reinforce.pdf]

M.A.M. Banaclocha, I. Bóokkon & H.M. Banaclocha (2010) Long-term memory in brain magnetite. Medical Hypotheses. 74(2), 254-257.

K. Bartkiewicz, A. Cernoch, G. Chimczak, K. Lemr, A. Miranowicz & F. Nori (2016) Experimental quantum forgery of quantum optical money. arXiv:1604.04453v1 [quant-ph]. Adam Mickiewicz University.

S. Bellinger (2005) Modeling calcium wave oscillations in astrocytes. Neurocomputing. 65(66), 843-850.

F. Black & M. Scholes (1973) The pricing of options and corporate liabilities. The Journal of Political Economy. 81(3), 637-659.

F. Briggs, G.R. Mangun & W.M. Usrey (2013) Attention enhances synaptic efficacy and the signal-to-noise ratio in neural circuits. Nature. 000, 1-5. [URL http://dx.doi.org/10.1038/nature12276]

L. Citi, R. Poli & C. Cinel (2010) Documenting, modelling and exploiting P300 amplitude changes due to variable target delays in Donchin's speller. Journal of Neural Engineering. 7(056006), 1-21. [URL http://dx.doi.org/10.1088/1741-2560/7/5/056006]

J. Conway & S. Kochen (2006) The free will theorem. arXiv:quant-ph/0604079 [quant-ph]. Princeton U.

J. Conway & S. Kochen (2009) The strong free will theorem. Notices of the American Mathematical Society. 56(2), 226-232.

K.A. Ericsson & W.G. Chase (1982) Exceptional memory. American Scientist. 70, 607-615.

P. Facchi, D.A. Lidar & S. Pascazio (2004) Unification of dynamical decoupling and the quantum Zeno effect. Physical Review A. 69(032314), 1-6.

P. Facchi & S. Pascazio (2008) Quantum Zeno dynamics: mathematical and physical aspects. Journal of Physics A. 41(493001), 1-45.

G. Giacosa & G. Pagliara (2014) Quantum Zeno effect by general measurements. Physical Review A. 052107, 1-5.

A.L. Goldberger, L.A.N. Amaral, L. Glass, J.M. Hausdorff, P.Ch. Ivanov, R.G. Mark, J.E. Mietus, G.B. Moody, C.-K. Peng & H.E. Stanley (2000) PhysioBank, PhysioToolkit, and PhysioNet: Components of a New Research Resource for Complex Physiologic Signals. Circulation. 101(23), e215-e220. [URL http://circ.ahajournals.org/cgi/content/full/101/23/e215]

S. Hagan, S.R. Hameroff & J.A. Tuszynski (2002) Quantum computation in brain microtubules: Decoherence and biological feasibility. Physical Review E. 65(061901), 1-11. [URL http://link.aps.org/doi/10.1103/PhysRevE.65.061901]

S. Hameroff & R. Penrose (2013) Consciousness in the universe: A review of the 'Orch OR' theory. Physics of Life Reviews. 403, 1-40. [URL http://dx.doi.org/10.1016/j.plrev.2013.08.002]

W. Hick (1952) On the rate of gains of information. Quarterly Journal Experimental Psychology. 34(4), 1-33.

J.C. Hull (2000) Options, Futures, and Other Derivatives, 4th Edition. Prentice Hall, Upper Saddle River, NJ.

L. Ingber (1981) Towards a unified brain theory. Journal Social Biological Structures. 4, 211-224. [URL https://www.ingber.com/smni81_unified.pdf]

L. Ingber (1982) Statistical mechanics of neocortical interactions. I. Basic formulation. Physica D. 5, 83-107. [URL https://www.ingber.com/smni82_basic.pdf]

L. Ingber (1983) Statistical mechanics of neocortical interactions. Dynamics of synaptic modification. Physical Review A. 28, 395-416. [URL https://www.ingber.com/smni83_dynamics.pdf]

L. Ingber (1984) Statistical mechanics of neocortical interactions. Derivation of short-term-memory capacity. Physical Review A. 29, 3346-3358. [URL https://www.ingber.com/smni84_stm.pdf]

L. Ingber (1985a) Statistical mechanics of neocortical interactions. EEG dispersion relations. IEEE Transactions in Biomedical Engineering. 32, 91-94. [URL https://www.ingber.com/smni85_eeg.pdf]

L. Ingber (1985b) Statistical mechanics of neocortical interactions: Stability and duration of the 7+-2 rule of short-term-memory capacity. Physical Review A. 31, 1183-1186. [URL https://www.ingber.com/smni85_stm.pdf]

L. Ingber (1985c) Towards clinical applications of statistical mechanics of neocortical interactions. Innovations Technology Biology Medicine. 6, 753-758.

L. Ingber (1989) Very fast simulated re-annealing. Mathematical Computer Modelling. 12(8), 967-973. [URL https://www.ingber.com/asa89_vfsr.pdf]

L. Ingber (1990) Statistical mechanical aids to calculating term structure models. Physical Review A. 42(12), 7057-7064. [URL https://www.ingber.com/markets90_interest.pdf]

L. Ingber (1991) Statistical mechanics of neocortical interactions: A scaling paradigm applied to electroencephalography. Physical Review A. 44(6), 4017-4060. [URL https://www.ingber.com/smni91_eeg.pdf]

L. Ingber (1992) Generic mesoscopic neural networks based on statistical mechanics of neocortical interactions. Physical Review A. 45(4), R2183-R2186. [URL https://www.ingber.com/smni92_mnn.pdf]

L. Ingber (1993a) Adaptive Simulated Annealing (ASA). Global optimization C-code. Caltech Alumni Association. [URL https://www.ingber.com/#ASA-CODE]

L. Ingber (1993b) Simulated annealing: Practice versus theory. Mathematical Computer Modelling. 18(11), 29-57. [URL https://www.ingber.com/asa93_sapvt.pdf]

L. Ingber (1993c) Statistical mechanics of combat and extensions, In: Toward a Science of Command, Control, and Communications, ed. C. Jones. American Institute of Aeronautics and Astronautics, 117-149. [ISBN 1-56347-068-3. URL https://www.ingber.com/combat93_c3sci.pdf]

L. Ingber (1994) Statistical mechanics of neocortical interactions: Path-integral evolution of short-term memory. Physical Review E. 49(5B), 4652-4664. [URL https://www.ingber.com/smni94_stm.pdf]

L. Ingber (1995a) Path-integral evolution of multivariate systems with moderate noise. Physical Review E. 51(2), 1616-1619. [URL https://www.ingber.com/path95_nonl.pdf]

L. Ingber (1995b) Statistical mechanics of multiple scales of neocortical interactions, In: Neocortical Dynamics and Human EEG Rhythms, ed. P.L. Nunez. Oxford University Press, 628-681. [ISBN 0-19-505728-7. URL https://www.ingber.com/smni95_scales.pdf]

L. Ingber (1995c) Statistical mechanics of neocortical interactions: Constraints on 40 Hz models of short-term memory. Physical Review E. 52(4), 4561-4563. [URL https://www.ingber.com/smni95_stm40hz.pdf]

L. Ingber (1996a) Adaptive simulated annealing (ASA): Lessons learned. Control and Cybernetics. 25(1), 33-54. [Invited paper to Control and Cybernetics on Simulated Annealing Applied to Combinatorial Optimization. URL https://www.ingber.com/asa96_lessons.pdf]

L. Ingber (1996b) Canonical momenta indicators of financial markets and neocortical EEG, In: Progress in Neural Information Processing, ed. S.-I. Amari, L. Xu, I. King & K.-S. Leung. Springer, 777-784. [Invited paper to the 1996 International Conference on Neural Information Processing (ICONIP'96), Hong Kong, 24-27 September 1996. ISBN 981-3083-05-0. URL https://www.ingber.com/markets96_momenta.pdf]

L. Ingber (1996c) Statistical mechanics of neocortical interactions: Multiple scales of EEG, In: Frontier Science in EEG: Continuous Waveform Analysis (Electroencephal. clin. Neurophysiol. Suppl. 45), ed. R.M. Dasheiff & D.J. Vincent. Elsevier, 79-112. [Invited talk to Frontier Science in EEG Symposium, New Orleans, 9 Oct 1993. ISBN 0-444-82429-4. URL https://www.ingber.com/smni96_eeg.pdf]

L. Ingber (1997a) EEG Database. UCI Machine Learning Repository, Irvine, CA. [URL http://archive.ics.uci.edu/ml/datasets/EEG+Database]

L. Ingber (1997b) Statistical mechanics of neocortical interactions: Applications of canonical momenta indicators to electroencephalography. Physical Review E. 55(4), 4578-4593. [URL https://www.ingber.com/smni97_cmi.pdf]

L. Ingber (1998a) Data mining and knowledge discovery via statistical mechanics in nonlinear stochastic systems. Mathematical Computer Modelling. 27(3), 9-31. [URL https://www.ingber.com/path98_datamining.pdf]

L. Ingber (1998b) Statistical mechanics of neocortical interactions: Training and testing canonical momenta indicators of EEG. Mathematical Computer Modelling. 27(3), 33-64. [URL https://www.ingber.com/smni98_cmi_test.pdf]

L. Ingber (1999) Statistical mechanics of neocortical interactions: Reaction time correlates of the g factor. Psycholoquy. 10(068). [Invited commentary on The g Factor: The Science of Mental Ability by Arthur Jensen. URL https://www.ingber.com/smni99_g_factor.pdf]

L. Ingber (2000) High-resolution path-integral development of financial options. Physica A. 283(3-4), 529-558. [URL https://www.ingber.com/markets00_highres.pdf]

L. Ingber (2005) Trading in Risk Dimensions (TRD). Report 2005:TRD. Lester Ingber Research. [URL https://www.ingber.com/markets05_trd.pdf]

L. Ingber (2006) Statistical mechanics of neocortical interactions: Portfolio of physiological indicators. Report 2006:PPI. Lester Ingber Research. [URL https://www.ingber.com/smni06_ppi.pdf]

L. Ingber (2009a) Statistical mechanics of neocortical interactions: Nonlinear columnar electroencephalography. NeuroQuantology Journal. 7(4), 500-529. [URL https://www.ingber.com/smni09_nonlin_column_eeg.pdf]

L. Ingber (2009b) Statistical mechanics of neocortical interactions: Portfolio of physiological indicators. The Open Cybernetics Systemics Journal. 3(14), 13-26. [URL http://dx.doi.org/10.2174/1874110x00903010013]

L. Ingber (2011) Computational algorithms derived from multiple scales of neocortical processing, In: Pointing at Boundaries: Integrating Computation and Cognition on Biological Grounds, ed. A. Pereira, Jr., E. Massad & N. Bobbitt. Springer, 1-13. [Invited Paper. URL https://www.ingber.com/smni11_cog_comp.pdf and http://dx.doi.org/10.1007/s12559-011-9105-4]

L. Ingber (2012a) Adaptive Simulated Annealing, In: Stochastic global optimization and its applications with fuzzy adaptive simulated annealing, ed. H.A. Oliveira, Jr., A. Petraglia, L. Ingber, M.A.S. Machado & M.R. Petraglia. Springer, 33-61. [Invited Paper. URL

https://www.ingber.com/asa11_options.pdf]

L. Ingber (2012b) Columnar EEG magnetic influences on molecular development of short-term memory, In: Short-Term Memory: New Research, ed. G. Kalivas & S.F. Petralia. Nova, 37-72. [Invited Paper. URL https://www.ingber.com/smni11_stm_scales.pdf]

L. Ingber (2012c) Influence of macrocolumnar EEG on Ca waves. Current Progress Journal. 1(1), 4-8. [URL https://www.ingber.com/smni12_vectpot.pdf]

L. Ingber (2013) Electroencephalographic (EEG) influence on Ca2+ waves: Lecture plates. Report 2013:LEFI. Lester Ingber Research. [2nd World Neuroscience Online Conference 18 June 2013. URL https://www.ingber.com/smni13_eeg_ca_lect.pptx and https://www.ingber.com/smni13_eeg_ca_lect.pdf]

L. Ingber (2015) Calculating consciousness correlates at multiple scales of neocortical interactions, In: Horizons in Neuroscience Research, ed. A. Costa & E. Villalba. Nova, 153-186. [ISBN: 978-1-63482-632-7. Invited paper. URL https://www.ingber.com/smni15_calc_conscious.pdf]

L. Ingber (2016a) Path-integral quantum PATHTREE and PATHINT algorithms. International Journal of Innovative Research in Information Security. 3(5), 1-15. [URL https://www.ingber.com/path16_quantum_path.pdf]

L. Ingber (2016b) Statistical mechanics of neocortical interactions: Large-scale EEG influences on molecular processes. Journal of Theoretical Biology. 395, 144-152. [URL https://www.ingber.com/smni16_large-scale_molecular.pdf and http://dx.doi.org/10.1016/j.jtbi.2016.02.003]

L. Ingber (2017a) Evolution of regenerative Ca-ion wave-packet in neuronal-firing fields: Quantum path-integral with serial shocks. International Journal of Innovative Research in Information Security. 4(2), 14-22. [URL https://www.ingber.com/path17_quantum_pathint_shocks.pdf]

L. Ingber (2017b) Options on quantum money: Quantum path-integral with serial shocks. International Journal of Innovative Research in Information Security. 4(2), 7-13. [URL https://www.ingber.com/path17_quantum_options_shocks.pdf]

L. Ingber (2017c) Quantum Path-Integral qPATHINT Algorithm. The Open Cybernetics Systemics Journal. 11, 119-133. [URL https://www.ingber.com/path17_qpathint.pdf and http://dx.doi.org/10.2174/1874110X01711010119]

L. Ingber (2018) Quantum Variables in Finance and Neuroscience II. Report 2018:FNQV. Lester Ingber Research. [URL https://www.ingber.com/path18_qpathint.pdf]

L. Ingber, C. Chen, R.P. Mondescu, D. Muzzall & M. Renedo (2001) Probability tree algorithm for general diffusion processes. Physical Review E. 64(5), 056702-056707. [URL https://www.ingber.com/path01_pathtree.pdf]

L. Ingber, H. Fujio & M.F. Wehner (1991) Mathematical comparison of combat computer models to exercise data. Mathematical Computer Modelling. 15(1), 65-90. [URL https://www.ingber.com/combat91_data.pdf]

L. Ingber & R.P. Mondescu (2003) Automated internet trading based on optimized physics models of markets, In: Intelligent Internet-Based Information Processing Systems, ed. R.J. Howlett, N.S. Ichalkaranje, L.C. Jain & G. Tonfoni. World Scientific, 305-356. [Invited paper. URL https://www.ingber.com/markets03_automated.pdf]

L. Ingber & P.L. Nunez (1995) Statistical mechanics of neocortical interactions: High resolution path-integral calculation of short-term memory. Physical Review E. 51(5), 5074-5083. [URL https://www.ingber.com/smni95_stm.pdf]

L. Ingber & P.L. Nunez (2010) Neocortical Dynamics at Multiple Scales: EEG Standing Waves, Statistical Mechanics, and Physical Analogs. Mathematical Biosciences. 229, 160-173. [URL https://www.ingber.com/smni10_multiple_scales.pdf]

L. Ingber, M. Pappalepore & R.R. Stesiak (2014) Electroencephalographic field influence on calcium momentum waves. Journal of Theoretical Biology. 343, 138-153. [URL https://www.ingber.com/smni14_eeg_ca.pdf and http://dx.doi.org/10.1016/j.jtbi.2013.11.002]

L. Ingber & B. Rosen (1992) Genetic algorithms and very fast simulated reannealing: A comparison. Mathematical Computer Modelling. 16(11), 87-100. [URL https://www.ingber.com/asa92_saga.pdf]

L. Ingber, R. Srinivasan & P.L. Nunez (1996) Path-integral evolution of chaos embedded in noise: Duffing neocortical analog. Mathematical Computer Modelling. 23(3), 43-53. [URL https://www.ingber.com/path96_duffing.pdf]

L. Ingber & J.K. Wilson (1999) Volatility of volatility of financial markets. Mathematical Computer Modelling. 29(5), 39-57. [URL https://www.ingber.com/markets99_vol.pdf]

L. Ingber & J.K. Wilson (2000) Statistical mechanics of financial markets: Exponential modifications to Black-Scholes. Mathematical Computer Modelling. 31(8/9), 167-192. [URL https://www.ingber.com/markets00_exp.pdf]

B. Innocenti, V. Parpura & P.G. Haydon (2000) Imaging extracellular waves of glutamate during calcium signaling in cultured astrocytes. Journal of Neuroscience. 20(5), 1800-1808.

A. Jensen (1987) Individual differences in the Hick paradigm, In: Speed of Information-Processing and Intelligence, ed. P.A. Vernon. Ablex, 101-175.

J. Jogenfors (2016) Quantum bitcoin: An anonymous and distributed currency secured by the no-cloning theorem of quantum mechanics. arXiv:1604.01383 [quant-ph]. Linkoping U.

W. Kozlowski, S.F. Caballero-Benitez & I.B. Mekhov (2015) Non-Hermitian dynamics in the quantum Zeno limit. arXiv:1510.04857 [quant-ph]. U Oxford.

F. Langouche, D. Roekaerts & E. Tirapegui (1979) Discretization problems of functional integrals in phase space. Physical Review D. 20, 419-432.

F. Langouche, D. Roekaerts & E. Tirapegui (1982) Functional Integration and Semiclassical Expansions. Reidel, Dordrecht, The Netherlands.

L.K. McKemmish, J.R. Reimers, R.H. McKenzie, A.E. Mark & N.S. Hush (2009) Penrose-Hameroff orchestrated objective-reduction proposal for human consciousness is not biologically feasible. Physical Review E. 80(021912), 1-6. [URL http://link.aps.org/doi/10.1103/PhysRevE.80.021912]

K. Meyer (2009) Extending and simulating the quantum binomial options pricing model. Thesis. U Manitoba. [URL http://hdl.handle.net/1993/3154]

M.M. Muller, S. Gherardini & F. Caruso (2016) Quantum Zeno Dynamics through stochastic protocols. arXiv:1607.08871v1 [quant-ph]. U Florence.

S. Murakami & Y. Okada (2006) Contributions of principal neocortical neurons to magnetoencephalography and electroencephalography signals. Journal of Physiology. 575(3), 925-936.

P.L. Nunez & R. Srinivasan (2006) Electric Fields of the Brain: The Neurophysics of EEG, 2nd Ed.. Oxford University Press, London.

P.L. Nunez, R. Srinivasan & L. Ingber (2013) Theoretical and experimental electrophysiology in human neocortex: Multiscale correlates of conscious experience, In: Multiscale Analysis and Nonlinear Dynamics: From genes to the brain, ed. M.M. Pesenson. Wiley, 149-178. [URL http://dx.doi.org/10.1002/9783527671632.ch06]

Y.S. Patil, S. Chakram & M. Vengalattore (2015) Measurement-induced localization of an ultracold lattice gas. Physical Review Letters. 115(140402), 1-5. [URL http://link.aps.org/doi/10.1103/PhysRevLett.115.140402]

A. Pereira, Jr. & F.A. Furlan (2009) On the role of synchrony for neuron-astrocyte interactions and perceptual conscious processing. Journal of Biological Physics. 35(4), 465-480.

J. Preskill (2015) Quantum Mechanics. Lecture Notes. Caltech. [http://www.theory.caltech.edu/people/preskill/ph219/]

R.C. Reyes & V. Parpura (2009) The trinity of Ca2+ sources for the exocytotic glutamate release from astrocytes. Neurochemistry International. 55(3), 1-14.

W.N. Ross (2012) Understanding calcium waves and sparks in central neurons. Nature Reviews Neuroscience. 13, 157-168.

R.F. Salazar, N.M. Dotson, S.L. Bressler & C.M. Gray (2012) Content-specific fronto-parietal synchronization during visual working memory. Science. 338(6110), 1097-1100. [URL http://dx.doi.org/10.1126/science.1224000]

E. Scemes & C. Giaume (2006) Astrocyte calcium waves: What they are and what they do. Glia. 54(7), 716-725. [URL http://dx.doi.org/10.1002/glia.20374]

L.S. Schulman (1981) Techniques and Applications of Path Integration. J. Wiley & Sons, New York.

K. Schulten (1999) Quantum Mechanics. Lecture Notes. U. Illinois. [URL http://www.ks.uiuc.edu/Services/Class/PHYS480/]

A. Volterra, N. Liaudet & I. Savtchouk (2014) Astrocyte Ca2+ signalling: an unexpected complexity. Nature Reviews Neuroscience. 15, 327-335.

M.F. Wehner & W.G. Wolfer (1983a) Numerical evaluation of path-integral solutions to Fokker-Planck equations. I.. Physical Review A. 27, 2663-2670.

M.F. Wehner & W.G. Wolfer (1983b) Numerical evaluation of path-integral solutions to Fokker-Planck equations. II. Restricted stochastic processes. Physical Review A. 28, 3003-3011.

M.F. Wehner & W.G. Wolfer (1987) Numerical evaluation of path integral solutions to Fokker-Planck equations. III. Time and functionally dependent coefficients. Physical Review A. 35, 1795-1801.

S.L. Wu, L.C. Wang & X.X. Yi (2012) Time-dependent decoherence-free subspace. Journal of Physics A. 405305, 1-11.

G. Zhang & H.A. Simon (1985) STM capacity for Chinese words and idioms: Chunking and acoustical loop hypotheses. Memory & Cognition. 13, 193-201.

P. Zhang, Q. Ai, Y. Li, D. Xu & C. Sun (2014) Dynamics of quantum Zeno and anti-Zeno effects in an open system. Science China Physics, Mechanics & Astronomy. 57(2), 194-207. [URL http://dx.doi.org/10.1007/s11433-013-5377-x]